

# Remote Material Characterization with Complex Baseband FMCW Radar Sensors

Ahmed M. Hegazy<sup>1, \*</sup>, Mostafa Alizadeh<sup>1</sup>, Amr Samir<sup>1</sup>,  
Mohamed Basha<sup>1, 2</sup>, and Safieddin Safavi-Naeini<sup>1</sup>

**Abstract**—This paper presents the theoretical basis and experimental validation for a technique to remotely characterize materials using FMCW radar sensors with complex baseband architecture. Our theoretical work proves that the magnitude and phase of the input reflection coefficient of a material can be accurately extracted from the baseband data of a complex-baseband FMCW radar. This complex reflection coefficient can be used to calculate the dielectric constant, loss tangent, thickness, and layer setup of a material with high accuracy due to the extra information obtained from the phase of the reflection coefficient. The analysis starts with a theoretical model for the complex reflection coefficient of a flat material slab suspended in air. We then introduce a formulation for the complex reflection coefficient existing in the complex baseband of an FMCW radar signal. We finally present the experimental testing performed using TI mmWave radar on two different material samples and introduce the test results for extracting the material dielectric properties and thickness using three different extraction methods compared against nominal values from literature. The test results prove the high accuracy of our technique resulting from the utilization of both magnitude and phase information of the input reflection coefficient, despite the relatively long free-space measurement distance and the multi-path reflections test environment.

## 1. INTRODUCTION

Material characterization has been a topic of interest in academia and research for a long time due to the need for an accurate and reliable information regarding material parameters and characteristics. Measuring the dielectric parameters of samples and materials is a very important process in various applications such as circuit board laminates, absorber materials characterization for microwave design, food quality control, production lines, and noninvasive health sensing applications [1–8]. Several techniques have been developed for extracting these dielectric parameters with the majority of them relying on the transmission and reflection coefficients of the material [3, 9, 10]. For resonance-based methods, the material sample is placed in a cavity resonator where the quality factor  $Q$  and resonance frequency of the cavity are monitored before and after placing the material inside the cavity [11]. Using these measurements, the complex permittivity of the material can be extracted. This method has a very high accuracy especially with low loss materials; however, it requires a high-end Vector Network Analyzer (VNA) for detecting the finest frequency shifts [2]. Other reported resonance-based techniques utilize split ring resonators fabricated on a microstrip line [12] and cavity fabricated into a substrate integrated waveguide substrate integrated waveguide (SIW) which can be used to characterize liquid samples [13]. The disadvantages of resonance-based methods are that they require preparation for the material samples to fit in the cavity resonators and that they are invasive techniques requiring a

---

*Received 24 March 2023, Accepted 30 June 2023, Scheduled 19 July 2023*

\* Corresponding author: Ahmed M. Hegazy (amhegazy@uwaterloo.ca).

<sup>1</sup> Centre for Intelligent Antenna and Radio Systems, University of Waterloo, Waterloo, Ontario, Canada. <sup>2</sup> CMC Microsystems, Ontario, Canada.

close contact with the material samples. Furthermore, they rely on expensive and bulky measurement instruments which makes them only convenient for lab usage.

On the other hand, One-Port method utilizes the reflection coefficient measurements for material samples placed as a termination for an open-ended waveguide. The reflection coefficient, which can be measured using a VNA, is altered by the presence of the material and hence contains information about the dielectric properties of that material sample, which can then be calculated by post-processing the VNA measured data. Different types of waveguide configurations can be used for this method, e.g., coaxial cables or rectangular waveguide. To translate the measurement reference plane to the end of the waveguide or the surface of the sample under test, a calibration or embedding has to be done before the measurement [2, 11]. Although it is non-destructive as no sample preparation is needed, one-port method requires direct contact with the material sample and is sensitive to any calibration error, e.g., air gap between the waveguide and the sample. An extension to one-port method is two-port method where both the reflection and transmission coefficients of the material under test are utilized for extracting the dielectric parameters [2, 11]. The two-port method is convenient for low loss materials and is also capable of extracting the permeability of the sample under test. The material sample, however, has to be shaped and placed inside the waveguide, hence it is considered a destructive method.

Free-space method has been extensively studied by many researchers due to the non-destructive and non-invasive nature of this technique which makes it favorable for applications where access to the material under test is restricted, e.g., industrial or production line applications [14–16]. Several setup configurations have been used for free-space material characterization depending on the transmitting and receiving antenna locations and whether the transmission or reflection coefficient is being measured [11]. One of the drawbacks of the free-space method is the multiple reflections from the test environment which can degrade the quality of the measured data. In [17], researchers developed a technique which mitigates this problem by performing multiple free-space measurements where the setup is rotated, and the measurement distance is changed with each test so that the measured data is averaged to cancel the multipath effects. Although it is effective in eliminating multipath effects in non-anechoic test environments, this technique requires large horn antennas and a bulky and expensive VNA to perform the testing. Another technique presented in [16] utilizes the radar cross-section (RCS) characteristics of the material sample under test to perform a dielectric constant measurement using a pulse generator and an oscilloscope. This technique does not require a flat material sample surface; however, it is still reliant on expensive lab equipment for the generation and processing of the test signal. The authors in [18] introduced another technique using a custom designed ultra-wideband (UWB) frequency modulated continuous wave (FMCW) radar with 50 GHz bandwidth and a real baseband architecture in contrast to our system which uses a low-cost commercial off-the-shelf board with lower bandwidth to achieve high accuracy from the phase information.

In this paper, we present a new free-space material characterization technique which utilizes the complex reflection coefficient extracted from the complex baseband of a commercial and low-cost TI AWR2243 FMCW radar operating at 77 GHz band with 5 GHz bandwidth. The information extracted from the magnitude and phase of the reflection coefficient is used to accurately extract the dielectric parameters and the thickness of the material under test. Additionally, the phase information can be used to identify the material layer configuration. This technique can extract the dielectric parameters accurately over a relatively long measurement distance and in a non-anechoic environment [19].

Compared to the methods discussed earlier, our system is portable, cheaper and utilizes a commercial TI radar chip to achieve very high characterization accuracy in a multi-reflection environment at longer measurement distances.

In Section 2, a theoretical basis for the flat material slab model is presented. Moreover, a rigorous theoretical model for the baseband signal of a complex baseband FMCW radar is introduced. Section 3 discusses the the different methods used for extracting the dielectric parameters of the material from the measured data. In Section 4, the radar board and lens antenna design used for the test setup are explained. The complete test setup and testing results are presented in Section 5. Finally, a conclusion for the work is introduced in Section 6.

## 2. THEORETICAL MODELLING AND ANALYSIS

Our proposed test setup shown in Figure 1 assumes a radar board with the Tx and Rx antennas pointed normally at the material sample from the same direction with a plane wave incidence, hence, the reflection coefficient of the material is received by the radar. We start our problem modelling by assuming a flat dielectric material sample with a finite thickness  $d$  backed by air as seen in Figure 2. Two equivalent models for the reflection coefficient at the material surface ( $z = -d$ ) are discussed: Transmission line model and multiple reflections model.

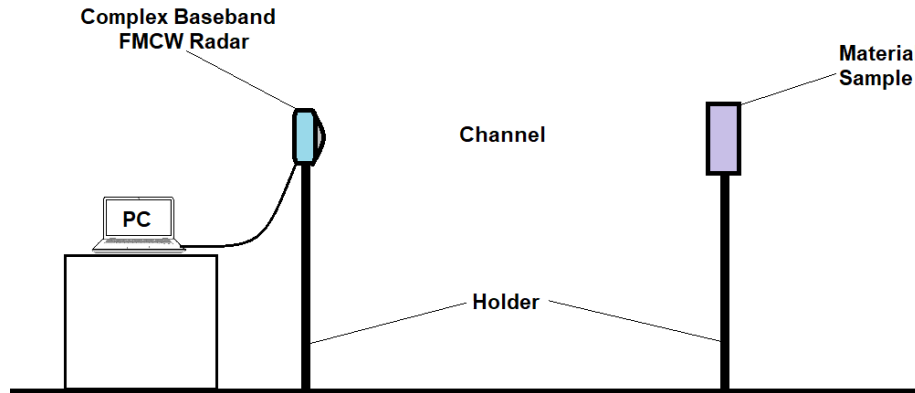


Figure 1. Proposed material characterization setup.

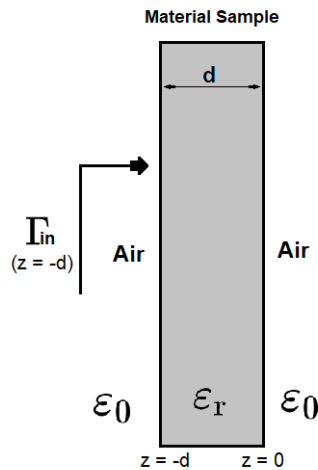
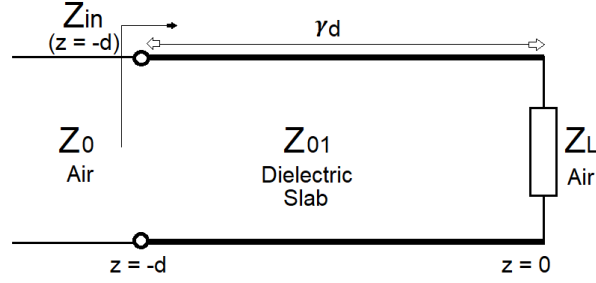


Figure 2. Model for flat dielectric slab with finite thickness backed by air.

### 2.1. Transmission Line Model

For the transmission line model, the material sample is modeled as a lossy transmission line with electrical length  $\gamma d$ , where  $\gamma$  is the propagation constant, and characteristic impedance  $Z_{01}$ , terminated by a load Impedance  $Z_L$ . This load impedance represents the backing layer behind the material sample. The air layer in front of the material is represented by an infinite length transmission line with characteristic impedance  $Z_0$  connected to the material transmission line at ( $z = -d$ ) as seen in Figure 3.

The characteristic impedance of the air layer  $Z_0$  is almost equal to free space impedance (376.7 Ohms), while the characteristic impedance of the dielectric slab  $Z_{01}$  is a function of the complex



**Figure 3.** Transmission line model for flat dielectric slab with finite thickness backed by air.

permittivity of the material as shown in the following formula:

$$Z_{01} = Z_0 \cdot \sqrt{\frac{1}{\epsilon_r}} \quad (1)$$

The input impedance of the material equivalent transmission line can then be calculated using the following formula:

$$Z_{in}(z = -d) = Z_{01} \left( \frac{Z_L + Z_{01} \cdot \tanh(\gamma d)}{Z_{01} + Z_L \cdot \tanh(\gamma d)} \right) \quad (2)$$

Finally, the input reflection coefficient at the surface of the dielectric slab ( $z = -d$ ) is equal to

$$\Gamma_{in}(z = -d) = \frac{Z_{in} - Z_0}{Z_{in} + Z_0} \quad (3)$$

Due to the simplicity of this model, it can be easily extended to multilayer material samples by inserting additional transmission lines with the respective characteristic impedance to represent the extra layers. For example, a two-layer material sample can be modeled as two cascaded transmission lines as seen in Figure 4.

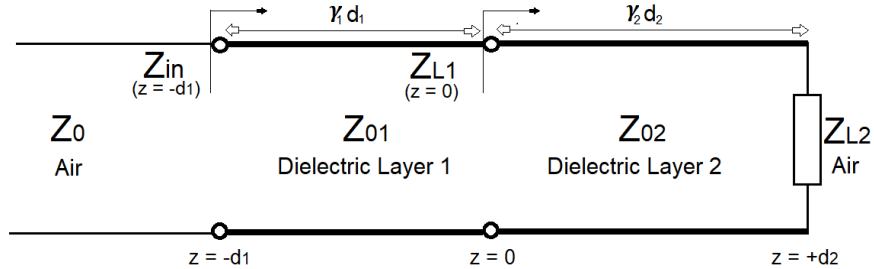


**Figure 4.** Transmission line model for multi-layer flat dielectric slab with finite thickness surrounded by air.

The input reflection coefficient can be derived as shown in the following set of equations:

$$Z_{02} = Z_0 \cdot \sqrt{\frac{1}{\epsilon_{r2}}} \quad (4)$$

$$Z_{L1}(z = 0) = Z_{02} \left( \frac{Z_{L2} + Z_{02} \cdot \tanh(\gamma_2 d_2)}{Z_{02} + Z_{L2} \cdot \tanh(\gamma_2 d_2)} \right) \quad (5)$$

$$Z_{in}(z = -d_1) = Z_{01} \left( \frac{Z_{L1} + Z_{01} \cdot \tanh(\gamma_1 d_1)}{Z_{01} + Z_{L1} \cdot \tanh(\gamma_1 d_1)} \right) \quad (6)$$

$$\Gamma_{in}(z = -d_1) = \frac{Z_{in} - Z_0}{Z_{in} + Z_0} \quad (7)$$

### 2.2. Multiple Reflections Model

The second model is the multiple reflections model which is similar to the Fabry-Pérot etalon method commonly used in photonics. In this model, a plane wave with a normalized amplitude of 1 is assumed to be normally incident on the surface a dielectric slab with thickness  $d$  as seen in Figure 5. Upon the wave incidence, part of the wave is reflected off the slab surface due to the permittivity contrast between air layer with the relative permittivity  $\approx 1$  and the material with relative permittivity  $\epsilon_r$  [20].

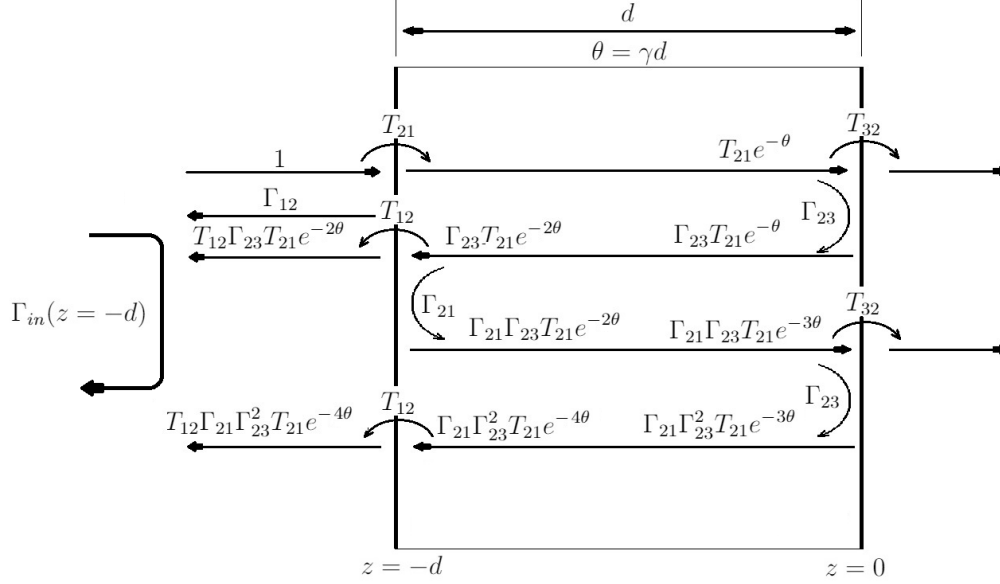


**Figure 5.** Transmissions and reflections inside a dielectric slab with finite thickness.

The reflected portion of the wave at the first incidence is a function of the dielectric constant of the material as shown in the following equation:

$$\Gamma_{12} = \frac{1 - \sqrt{\epsilon_r}}{1 + \sqrt{\epsilon_r}} \quad (8)$$

The transmitted portion, expressed as  $T_{21} = 1 + \Gamma_{12}$ , is then transmitted through the slab thickness to the other interface at ( $z = 0$ ), affected by the propagation constant  $\gamma$ . A continuous transmission and reflection are then repeated indefinitely between the two interfaces of the slab. The input reflection coefficient at the first slab interface  $\Gamma_{in}(z = -d)$  is the sum of all the reflected transmission and reflection components at ( $z = -d$ ) as shown in following equations:

$$\Gamma_{in}(z = -d) = \Gamma_{12} + T_{12}\Gamma_{23}T_{21}e^{-2\theta} + T_{12}\Gamma_{21}\Gamma_{23}^2T_{21}e^{-4\theta} + \dots \quad (9)$$

$$\Gamma_{in}(z = -d) = \Gamma_{12} + T_{12}\Gamma_{23}T_{21}e^{-2\theta} \left( 1 + \Gamma_{21}\Gamma_{23}e^{-2\theta} + \left( \Gamma_{21}\Gamma_{23}e^{-2\theta} \right)^2 + \dots \right) \quad (10)$$

$$\Gamma_{in}(z = -d) = \frac{\Gamma_{12} + \Gamma_{23}e^{-2\gamma d}}{1 + \Gamma_{12}\Gamma_{23}e^{-2\gamma d}} \quad (11)$$

$$\Gamma_{23} = -\Gamma_{12} \quad (12)$$

Finally, the following equation is a closed form expression for  $\Gamma_{in}(z = 0)$ :

$$\Gamma_{in}(z = -d) = \frac{\Gamma_{12}(1 - e^{-2\gamma d})}{1 - \Gamma_{12}^2 e^{-2\gamma d}} \quad (13)$$

where

$$\gamma = \alpha + j\beta \quad (14)$$

$$\beta = \frac{2\pi\sqrt{\varepsilon_r}}{\lambda}, \quad (\text{for } \tan \delta \ll 1) \quad (15a)$$

$$\alpha = \frac{\pi\sqrt{\varepsilon_r}}{\lambda} \tan \delta, \quad (\text{for } \tan \delta \ll 1) \quad (16a)$$

### 2.3. FMCW Model

Frequency modulated continuous wave (FMCW) radar is a special radar technique which utilizes a waveform that is frequency modulated over time for measuring the range and speed of a target. This frequency-modulated waveform, also known as *Chirp*, is usually generated using a voltage controlled oscillator (VCO) driven by a periodic modulating voltage signal, e.g., linear ramp or sawtooth. The chirp signal is then transmitted to the target and reflected back after a specific time which is proportional to the target distance [21, 22]. The received chirp is then mixed with the conjugate of the chirp being transmitted, low pass filtered, and finally transformed to the frequency domain through Fast Fourier Transform (FFT), generating a baseband signal known as the *Beat*. This frequency of this beat signal is directly proportional to the distance of the target as seen in the following equation:

$$f_{beat} = \frac{2BR}{t_c c} \quad (17)$$

where  $f_{beat}$  is the frequency of the beat signal,  $B$  the bandwidth of the chirp signal,  $R$  the range of the target,  $t_c$  the chirp period, and finally  $c$  the speed of light.

In order to formulate the relationship of the input reflection coefficient of a material  $\Gamma_{in}$ , which represents the radar target, and the complex baseband beat signal for FMCW radar, we start with Equation (9) in the multiple reflections model. Assuming a lossy dielectric material, the slab thickness  $\theta = \gamma d$  can be expressed as  $\omega C_1 + j\omega C_2$  with  $C_1$  and  $C_2$  representing constant terms as shown in the following equations:

$$\begin{aligned} \theta = \gamma d &= (\alpha + j\beta) d = \left( \frac{\pi\sqrt{\varepsilon_r}}{\lambda} \tan \delta + j \frac{2\pi\sqrt{\varepsilon_r}}{\lambda} \right) d = \frac{\pi\sqrt{\varepsilon_r} \tan \delta}{\lambda} d + j \frac{2\pi\sqrt{\varepsilon_r}}{\lambda} d \\ &= \frac{\omega\sqrt{\varepsilon_r} \tan \delta}{2c} d + j \frac{\omega\sqrt{\varepsilon_r}}{c} d = \omega C_1 + j\omega C_2 \end{aligned} \quad (18)$$

where

$$C_1 = \frac{\sqrt{\varepsilon_r} \tan \delta}{2c} d, \quad (19)$$

$$C_2 = \frac{\sqrt{\varepsilon_r}}{c} d \quad (20)$$

Therefore, Equation (9) can then be expressed in frequency domain as seen below:

$$\Gamma_{in}(\omega) = \Gamma_{12} + T_{12}\Gamma_{23}T_{21}e^{-2\omega C_1}e^{-j2\omega C_2} + T_{12}\Gamma_{21}\Gamma_{23}^2T_{21}e^{-4\omega C_1}e^{-j4\omega C_2} + \dots \quad (21)$$

For simplicity, the constant reflection and transmission terms are represented as  $a_0, a_1, a_2, \dots$ , as follows:

$$\Gamma_{in}(\omega) = a_0 + a_1e^{-2\omega C_1}e^{-j2\omega C_2} + a_2e^{-4\omega C_1}e^{-j4\omega C_2} + \dots \quad (22)$$

The input reflection coefficient as a function of frequency  $\Gamma_{in}(\omega)$  can then be expressed as the following equation:

$$\Gamma_{in}(\omega) = \sum_{n=0}^{\infty} a_n e^{-2n\omega C_1} e^{-j2n\omega C_2} \quad (23)$$

The signal  $x(t)$ , representing the complex chirp generated by the FMCW radar, is transmitted by the radar towards the target with an amplitude  $A_0$  and an initial phase  $\theta_0$  as shown in the following equation:

$$x(t) = A_0 e^{j(\omega(t)t + \theta_0)} \quad (24)$$

where

$$\tau = \frac{2R}{c} \quad (25)$$

In the previous equation,  $\omega(t)$  represents the chirp's linear frequency variation starting from an initial frequency  $\omega_0$  with a frequency slope  $B/t_c$  as seen in the following equation:

$$\omega(t) = \omega_0 + \frac{B}{t_c} t \quad (26)$$

where  $B$  is the bandwidth of the chirp, and  $t_c$  is the chirp duration.

In the previous equation, it can be noted that there is an equivalency between the time and the frequency of the chirp. Using this equivalency, the time domain chirp  $x(t)$  can be expressed as a function of  $\omega$  as follows:

$$x(\omega) = A_0 e^{j(\omega^2 \frac{t_c}{B} - \omega \omega_0 \frac{t_c}{B} + \theta_0)} \quad (27)$$

This complex chirp reaches the target as  $x'(\omega)$ , delayed by a duration  $\tau/2$  resulting from the distance to target  $R$  as shown below:

$$x'(\omega) = x(\omega) \cdot e^{-j\omega \frac{\tau}{2}} = A_0 e^{j(\omega(t)^2 \frac{t_c}{B} - \omega(t)\omega_0 \frac{t_c}{B} - \omega \frac{\tau}{2} + \theta_0)} \quad (28)$$

This delayed chirp is then multiplied by the input reflection coefficient of the material  $\Gamma_{in}(\omega)$  resulting in signal  $y(\omega)$  which is then reflected back to the radar as  $y'(\omega)$  with another time delay  $\tau/2$  resulting from the distance from the material back to the radar as seen in the following equations:

$$y(\omega) = x'(\omega) \cdot \Gamma_{in}(\omega) = \left( A_0 e^{j(\omega(t)^2 \frac{t_c}{B} - \omega(t)\omega_0 \frac{t_c}{B} - \omega \frac{\tau}{2} + \theta_0)} \right) \cdot \left( \sum_{n=0}^{\infty} a_n e^{-2n\omega C_1} e^{-j2n\omega C_2} \right) \quad (29)$$

$$y(\omega) = A_0 \sum_{n=0}^{\infty} a_n e^{-2n\omega C_1} e^{-j(2n\omega C_2 - \omega(t)^2 \frac{t_c}{B} + \omega(t)\omega_0 \frac{t_c}{B} + \omega \frac{\tau}{2} - \theta_0)} \quad (30)$$

$$y'(\omega) = y(\omega) \cdot e^{-j\omega \frac{\tau}{2}} = A_0 \sum_{n=0}^{\infty} a_n e^{-2n\omega C_1} e^{-j(2n\omega C_2 - \omega(t)^2 \frac{t_c}{B} + \omega(t)\omega_0 \frac{t_c}{B} + \omega \tau - \theta_0)} \quad (31)$$

Due to the travelling time of the multiple reflection components seen in Figure 5 inside the material thickness, the frequency difference between these components has to be studied. We first derive the following formula for the time difference  $t_d$  due to the wave travelling time between the two material interfaces:

$$t_d = \frac{2nd\sqrt{\epsilon_r}}{c} \quad (32)$$

where  $n$  is the order of the reflection component. Using Equation (26), the frequency difference  $\Delta\omega$  corresponding to this time difference can be expressed as:

$$\Delta\omega = \frac{B}{t_c} t_d \quad (33)$$

For our system with an effective sweeping bandwidth of 4.41 GHz, the frequency error of the first frequency component is found to be 23.8 kHz which corresponds to a frequency error of 0.0005%. It is found from simulation that the first 4 reflection components are usually the main contributing terms in the input reflection coefficient, while the contribution of terms  $n > 3$  is negligible. Due to this small frequency error, the frequency of the different reflection components can be assumed to be constant with the frequency difference being neglected.

The received signal  $y'(\omega)$  is then mixed with the conjugate of the transmitted signal  $x(\omega)$ , generating the complex baseband signal  $z(\omega)$  as seen in the following equations:

$$\begin{aligned} z(\omega) &= y'(\omega) \cdot \overline{x(\omega)} \\ &= \left( A_0 \sum_{n=0}^{\infty} a_n e^{-2n\omega C_1} e^{-j(2n\omega C_2 - \omega(t)^2 \frac{t_c}{B} + \omega(t)\omega_0 \frac{t_c}{B} + \omega \tau - \theta_0)} \right) \cdot \left( A_0 e^{-j(\omega(t)^2 \frac{t_c}{B} - \omega(t)\omega_0 \frac{t_c}{B} + \theta_0)} \right) \end{aligned} \quad (34)$$

$$z(\omega) = A_0^2 \sum_{n=0}^{\infty} a_n e^{-2n\omega C_1} e^{-j(2n\omega C_2 - \omega(t)^2 \frac{t_c}{B} + \omega(t)\omega_0 \frac{t_c}{B} + \omega \tau - \theta_0 + \omega(t)^2 \frac{t_c}{B} - \omega(t)\omega_0 \frac{t_c}{B} + \theta_0)} \quad (35)$$

Finally, the phase terms  $\omega(t)^2 t_c/B$ ,  $\omega(t)\omega_0 t_c/B$  and the initial phase terms  $\theta_0$  cancel out resulting in the following formula:

$$z(\omega) = A_0^2 \sum_{n=0}^{\infty} a_n e^{-2n\omega C_1} e^{-j(2n\omega C_2 + \omega\tau)} \quad (36)$$

Compared to Equation (23), it is obvious that the complex baseband signal  $z(\omega)$  of the FMCW radar represents the input reflection coefficient  $\Gamma_{in}(\omega)$  with the magnitude scaled by  $A_0^2$  and the phase distorted by the additional linear phase distortion term  $\omega\tau$  resulting from the distance between the material and the radar. Additionally, the real exponential term  $e^{-2n\omega C_1}$  represents the attenuation resulting from the loss tangent of the material and is equal to 1 for lossless materials. In reality, the received signal  $y'(\omega)$  will also be affected by the gain of the Tx and Rx antennas, the channel path loss, and the RCS of the material sample.

#### 2.4. Calibration

To accurately extract the complex input reflection coefficient from the complex baseband signal of FMCW radar, de-embedding is essential for removing the magnitude and phase errors discussed before. The measurement setup can be modeled as a simple one port network which is terminated by a load representing the input impedance  $Z_{in}$  of the material under test (MUT) and its backing layers. All the magnitude and phase errors combined can be modeled as a two-port error network connecting the measurement system and the material interface as shown in Figure 6.

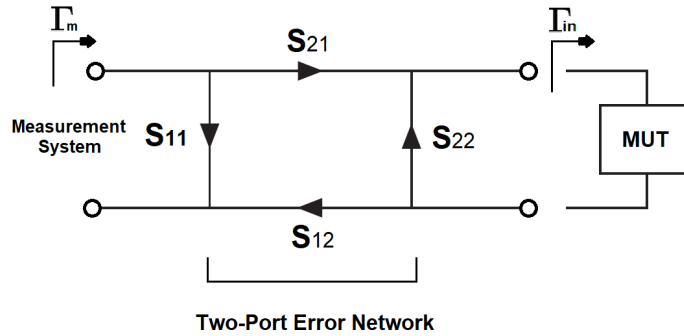


**Figure 6.** Signal flow diagram for the material under test (MUT) with the error network.

This error network can be de-embedded using one-port calibration technique commonly used in VNA measurements. To formulate this calibration technique, we first start with the input reflection coefficient seen by the measurement system  $\Gamma_m$  as a function of the input reflection coefficient of the material  $\Gamma_{in}$  and the  $S$  parameters of the error network as shown in the following equations:

$$\Gamma_m = S_{11} + \frac{S_{12}S_{21}\Gamma_{in}}{1 - S_{22}\Gamma_{in}} \quad (37)$$

$$\Gamma_{in} = \frac{\Gamma_m - S_{11}}{S_{12}S_{21} + S_{22}(\Gamma_m - S_{11})} \quad (38)$$

This means that knowing all the  $S$  parameters of the error network is essential for extracting the actual  $\Gamma_{in}$  of the material. The first step in the calibration process is extracting  $S_{11}$  by matching the load representing the material and hence setting  $\Gamma_{in}$  to zero in Equation (37), resulting in only  $S_{11}$ .

$$\Gamma_{m-match} = S_{11} \quad (39)$$

In the actual test, this step is implemented by removing the material sample from the setup and performing one input reflection coefficient measurement using the radar. The next step is replacing the

material with a metallic equivalent surface and therefore setting  $\Gamma_{in}$  to  $-1$  resulting in the following equation:

$$\Gamma_{m-short} = S_{11} - \frac{S_{12}S_{21}}{1 + S_{22}} = \Gamma_{m-match} - \frac{S_{12}S_{21}}{1 + S_{22}} \quad (40)$$

This metallic equivalent can then be shifted by a small known distance  $\Delta d$  resulting in a phase shift of  $2\omega \frac{\Delta d}{c}$ , and hence  $\Gamma_{in}$  becomes equal to  $-e^{j2\omega \frac{\Delta d}{c}}$  reaching the equation below:

$$\Gamma_{m-shift} = S_{11} - \frac{S_{12}S_{21}e^{j2\omega \frac{\Delta d}{c}}}{1 + S_{22}e^{j2\omega \frac{\Delta d}{c}}} = \Gamma_{m-match} - \frac{S_{12}S_{21}e^{j2\omega \frac{\Delta d}{c}}}{1 + S_{22}e^{j2\omega \frac{\Delta d}{c}}} \quad (41)$$

Using these equations, all the unknown  $S$  parameters in Equation (37) can be calculated, and finally  $\Gamma_{in}$  can be extracted from  $\Gamma_m$  measured by the radar. The actual implementation for these calibration steps is presented in the experimental results section below.

### 3. EXTRACTION OF DIELECTRIC PARAMETERS

After measuring the input reflection coefficient of the material, the next step is to extract the dielectric parameters and the thickness of the material sample from the measured  $\Gamma_{in}$ . Two methods are proposed in this section, the maxima and minima method and the curve fitting method. Both methods assume a frequency independent  $\epsilon_r$ .

#### 3.1. Maxima and Minima Method

Looking at  $\Gamma_{in}$  models discussed in the previous section and assuming a lossless material, it can be observed that the magnitude of  $\Gamma_{in}$  exhibits a unique periodic behavior over the frequency as shown in Figure 7. This periodic behavior results from the summation of the reflection components with different phases as seen in Equation (9). The location of the maxima and minima over the frequency axis and the value of the maxima are specific to the dielectric constant and the thickness of the material. This means that the characteristics of these minima and maxima can be considered as a fingerprint for the material with a specific thickness.

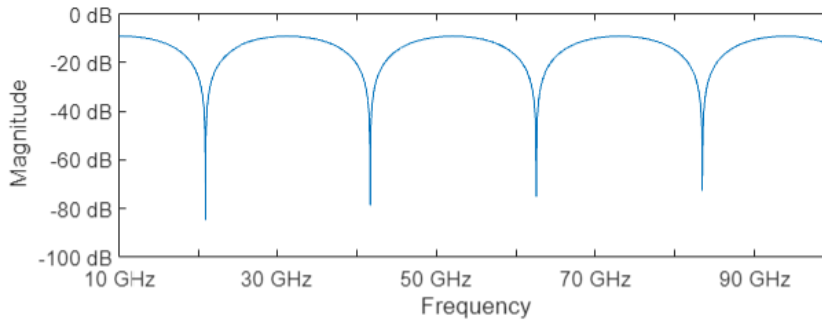


**Figure 7.** Simulated magnitude of  $\Gamma_{in}$  for a 5 mm thick Teflon sample using the transmission line model.

To derive the relationship between these minima and maxima characteristics and the dielectric constant and the thickness of the material, we start with the following equation for  $\Gamma_{in}$  of a lossless material derived from Equation (42) in the multiple reflections model:

$$\Gamma_{in} = \frac{\Gamma_{12}(1 - e^{-j2\beta d})}{1 - \Gamma_{12}^2 e^{-j2\beta d}} \quad (42)$$

The maximum of  $\Gamma_{in}$  occurs when the term  $e^{-j2\beta d}$  existing in the numerator and denominator of the previous equation is equal to  $-1$  resulting in the following equation [20]:

$$|\Gamma_{in}|_{\max} = \left| \frac{2\Gamma_{12}}{1 + \Gamma_{12}^2} \right| \quad (43)$$

Solving this equation for  $\Gamma_{12}$  results in 2 different solutions with one of them representing a valid solution for  $\Gamma_{12}$ . The dielectric constant  $\varepsilon_r$  can then be calculated using the following equation:

$$\varepsilon_r = \left( \frac{1 - \Gamma_{12}}{1 + \Gamma_{12}} \right)^2 \quad (44)$$

Similarly, the condition for the minima occurs when the term  $e^{-j2\beta d}$  is equal to 1, and therefore  $\Gamma_{in}$  is equal to zero. This particular condition occurs when  $2\beta d$  is equal to integer multiples of  $2\pi$  as seen in the following equation where  $n$  represents the order of the minima [20]:

$$2\beta d = 2n\pi \quad (45)$$

By further manipulation for the previous formula, we can reach the following two equations relating the dielectric constant  $\varepsilon_r$ , material thickness  $d$ , the frequency of minima  $f$ , minima order  $n$ , and the speed of light  $c$ .

$$\varepsilon_r = \left( \frac{nc}{2fd} \right)^2 \quad (46)$$

$$d = \frac{nc}{2f\sqrt{\varepsilon_r}} \quad (47)$$

By calculating the dielectric constant of the material using Equation (44), the thickness  $d$  can then be found using Equation (48) by knowing the frequency and the order of a minimum  $n$ . The order of a minimum  $n$  can be calculated by dividing the frequency of a minimum by the frequency difference of two subsequent minima or maxima as shown in the following equation:

$$n = \left( \frac{f_{\min}}{f_{\min(i)} - f_{\min(i-1)}} \right) = \left( \frac{f_{\max}}{f_{\max(i)} - f_{\max(i-1)}} \right) \quad (48)$$

This method is only valid for lossless dielectric materials. For highly lossy materials, the real part of the dielectric constant can be directly calculated using Equation (44) by knowing the magnitude of  $\Gamma_{12}$  that the magnitude of  $\Gamma_{in}$  eventually converges to.

### 3.2. Curve Fitting Method

The second method which can be used for extracting the dielectric properties and thickness from a measured  $\Gamma_{in}$  of a material is the nonlinear least square curve fitting method. The method works by searching for a solution  $x_i$  for the following function:

$$\min \left( \sum |F(x_i) - y_i|^2 \right) \quad (49)$$

where  $F(x_i)$  is a nonlinear function, and  $y_i$  represents the data to be fit. For our case, the nonlinear functions  $F(x_i)$  used for fitting are Equation (50) for the magnitude and Equation (51) for the phase:

$$|\Gamma_{in}| = \frac{\sqrt{(|\Gamma_{12}| - |\Gamma_{12}|e^{-2\alpha d} \cos 2\beta d)^2 + (|\Gamma_{12}|e^{-2\alpha d} \sin 2\beta d)^2}}{\sqrt{(1 - |\Gamma_{12}|^2 e^{-2\alpha d} \cos 2\beta d)^2 + (|\Gamma_{12}|^2 e^{-2\alpha d} \sin 2\beta d)^2}} \quad (50)$$

$$\angle \Gamma_{in} = \tan^{-1} \left( \frac{|\Gamma_{12}|e^{-2\alpha d} \sin 2\beta d}{|\Gamma_{12}|(1 - e^{-2\alpha d} \cos 2\beta d)} \right) - \tan^{-1} \left( \frac{|\Gamma_{12}|^2 e^{-2\alpha d} \sin 2\beta d}{1 - |\Gamma_{12}|^2 e^{-2\alpha d} \cos 2\beta d} \right) \quad (51)$$

Both these equations are derived from Equation (13) in the multiple reflection model.

This method is valid for both lossless and lossy materials and works for both the magnitude and phase information of  $\Gamma_{in}$  since both the magnitude and phase contain information regarding the dielectric properties and thickness of the material sample. This also means that the magnitude or the phase can be utilized separately either for the extraction or for extracting initial fitting values of the other for enhanced accuracy.

### 3.3. Phase Information and Layer Configuration

One of the benefits of utilizing the phase information along with the magnitude of  $\Gamma_{in}$  is the ability to identify the layer configuration for the material sample, e.g., suspended in air or placed on a metal substrate. For example, a metal sample and a lossless dielectric sample backed by metal have almost identical magnitude profile over frequency, while having a distinguishable unwrapped phase profile that can be used for identifying the configuration as shown in Figure 8.

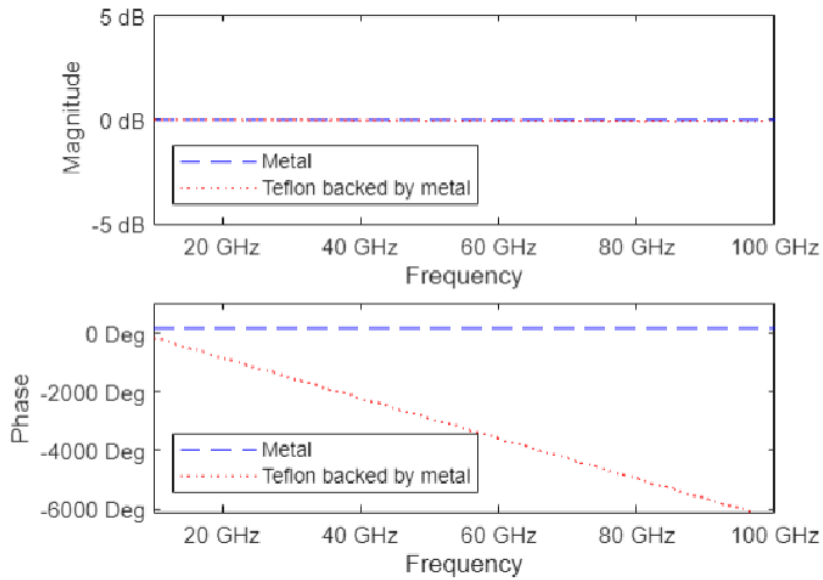


**Figure 8.** A comparison between the magnitude and the unwrapped phase of MATLAB simulated  $\Gamma_{in}$  for a metal sample and a teflon sample backed by metal.

## 4. RADAR BOARD

For our measurement setup, a commercial off-the-shelf TI AWR2243BOOST radar board, shown in Figure 13, is used. This board is mainly designed for automotive safety and radar imaging applications [21]. The radar transceiver chip covers a 5 GHz sweeping bandwidth ranging from 76 GHz up to 81 GHz. The radar chip also supports 3 Tx and 4 Rx channels with multiple-input multiple-output (MIMO) and phased array operation modes [23].

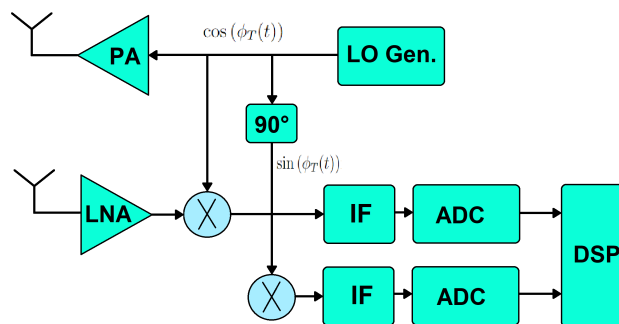


**Figure 9.** Block diagram for FMCW radar with complex baseband architecture.

#### 4.1. Complex Baseband Architecture

One of the key features of TI AWR2243 radar is the complex baseband architecture design. This baseband architecture is achieved through feeding the received signal to In-phase and Quadrature signal paths and mixing them with the instantaneous transmitted signal as shown in Figure 9.

This type of architecture improves the radar's tolerance to interference and lowers the impact of intermodulation. Most importantly, it gives us the ability to extract both the magnitude and the phase of the input reflection coefficient from the complex baseband signal of the radar [24].

#### 4.2. Antenna Frontend and Lens Design

The antenna front-end of the radar board is configured with 3 Tx and 4 Rx series-fed patch antennas with 2 dummy arrays as shown in Figure 10.

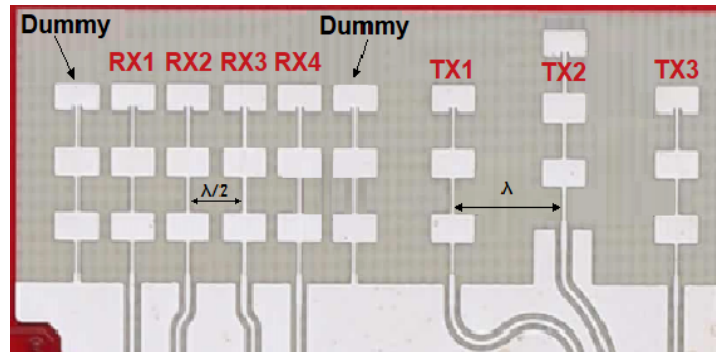


**Figure 10.** Antenna front-end for AWR2243BOOST radar board.

Due to the design of the series-fed arrays, the direction of the main beam exhibits a small vertical angular shift with frequency. This small frequency shift can introduce significant errors for our material characterization setup which assumes a normal incidence for the transmitted signal on the material surface. To solve this beam shifting problem, a dielectric lens antenna is designed for correcting the direction of the main beam while providing additional gain enhancement for maximum signal reflection from the material sample.

This dielectric lens is designed as a dual lens structure fed by the 3rd Tx antenna and received by the 1st Rx antenna as seen in Figure 11.

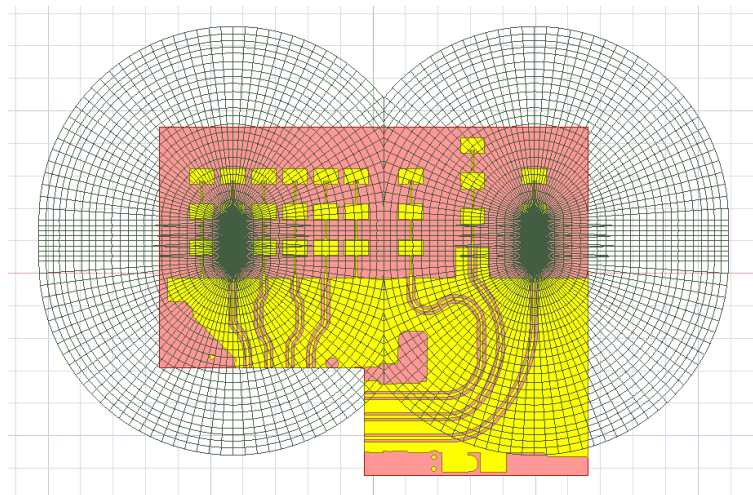


**Figure 11.** Top view for the dual lenses aligned to the on-board antennas underneath.

This lens design is based on a modified hyperbolic lens profile and fabricated using 3D-printing [25]. The simulation results seen in Figure 12 show the corrected main beam direction over the radar sweeping bandwidth.

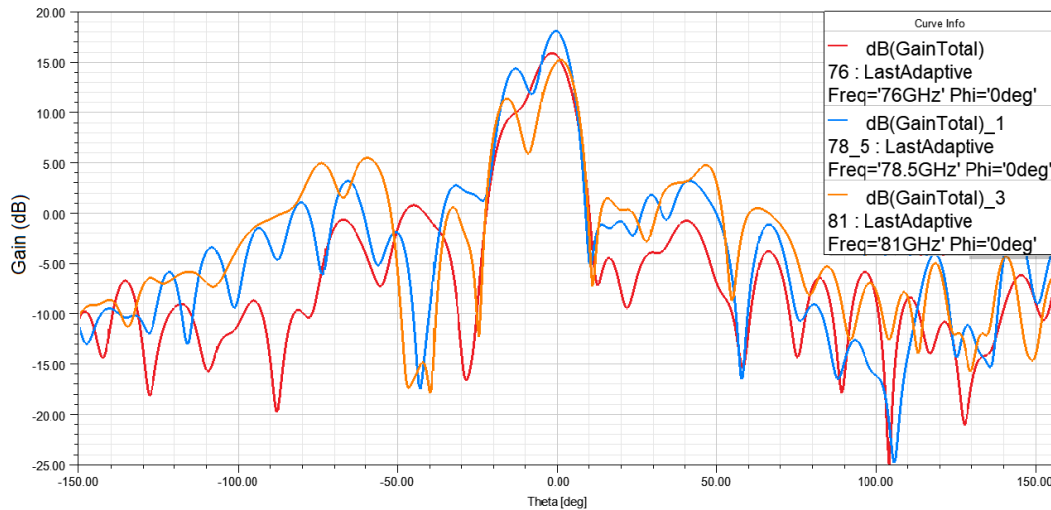


**Figure 12.** Simulation results of  $E$ -plane radiation pattern for single radar antenna with the hyperbolic lens structure for 76, 78.5 and 81 GHz.

The lens structure is mounted on the radar board using a 3D-printed adjustable fixture as shown in Figure 13. Due to the large ratio between the measurement distance between the radar and the material sample (2 m) and the distance between the Tx and Rx antennas ( $4\lambda$  at 77 GHz or 1.556 cm), the deviation angle of the reflected beam received at Rx antenna is around  $0.445^\circ$ . Therefore, the radar configuration can be assumed to be a monostatic radar.

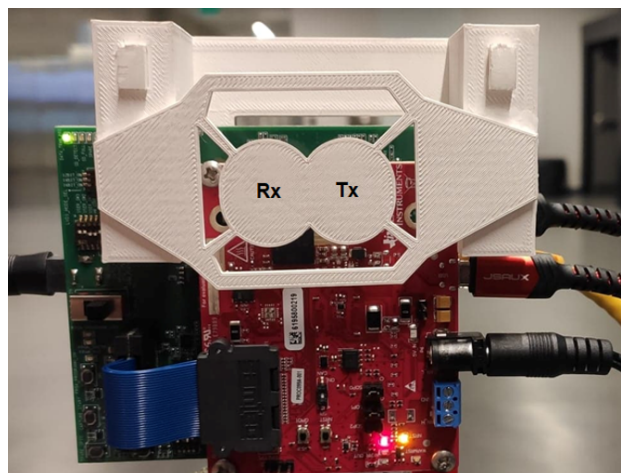


**Figure 13.** The dual lenses structure attached to the radar board through the holder.

## 5. EXPERIMENTAL RESULTS

In this section, we present the experimental setup used for measurement and the acquired results using different extractions methods compared against actual values from literature. Our measurements setup

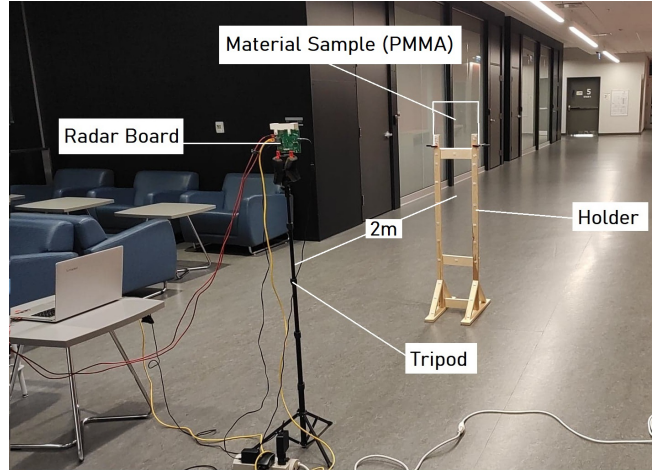


**Figure 14.** Experimental material characterization setup.

shown in Figure 14 consists of the TI AWR2243 radar board connected to PC through a USB and an Ethernet cable and mounted on an adjustable tripod. The material sample is a  $12'' \times 12''$  slab mounted on a fixed wooden holder.

Due to our assumption of a plane wave incidence on the surface of the material sample, the sample has to be placed in the far-field region of the Tx antenna aperture. This region is calculated to be at the distance greater than 42.3 cm using the Tx lens aperture of 28 mm and the highest frequency of the radar sweeping bandwidth of 81 GHz. This means that the distance between the radar and the sample has to be greater than 42.3 cm in order to validate our theoretical assumption. To strictly ensure this far-field rule and to maintain a normal incidence for the main beam of the lens antenna without any edge spilling, the material sample is placed 2 m away from the radar. It is worth mentioning that the accuracy, stability, and proper positioning and alignment of the radar sensor and material sample are crucial to obtaining accurate measurements.

### 5.1. Calibration

As discussed before, it is essential to perform a calibration process to de-embed all the magnitude and phase errors presenting from the channel and the radar system. The calibration process is an experimental implementation for the theoretical formulation presented earlier. The first step in the calibration process is to extract  $\Gamma_{m-match}$  which is achieved by measuring the reflection coefficient while the material sample is removed from the system. This measurement step is essential to removing any reflections occurring due to the measurement setup, e.g., the holder, or the surrounding environment. The second step is measuring  $\Gamma_{m-short}$  by replacing the material sample with a metallic equivalent (Aluminum) having the same dimension ( $12'' \times 12''$  as shown in Figure 15(a).

The final step is to measure  $\Gamma_{m-shift}$  by shifting the metallic equivalent back by a known distance  $\Delta d$  according to Equation (40). This shift is implemented by placing two 3D-printed plastic plates with 3 mm thickness between the metal plate and the holder as seen in Figure 15(b). It is worth mentioning that any thickness error in these calibration plates will produce a linear phase distortion of  $2\omega \frac{\Delta l}{c}$  where  $\Delta l$  is the error in the plate thickness. In our setup, the accuracy of the plate thickness is maintained by using a high accuracy 3D printer for fabricating the plates. To verify the quality of the calibration process, new  $\Gamma_{m-match}$  and  $\Gamma_{m-short}$  measurements are performed after the calibration as shown in Figure 16. The low reflection level of  $-40$  dB for  $\Gamma_{m-match}$  indicates the effectiveness of the calibration in removing the reflections and errors from the setup and the surrounding environment. Moreover, the 0 dB level of the short measurement indicates the excellent magnitude de-embedding and removal of the channel and FMCW magnitude errors.

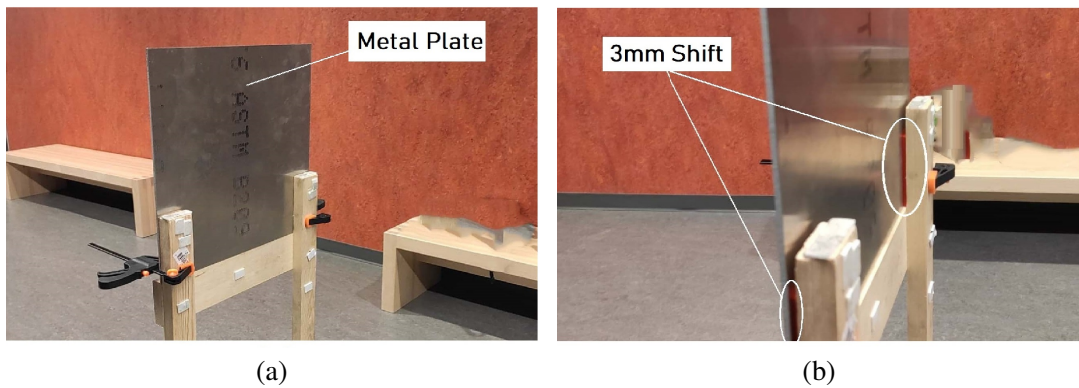


**Figure 15.** Calibration procedure. (a) Extracting  $\Gamma_{m-short}$  using metallic plate with the same dimensions of the material sample. (b) Extracting  $\Gamma_{m-line}$  by shifting the metallic plate using a 3 mm thick plastic piece.

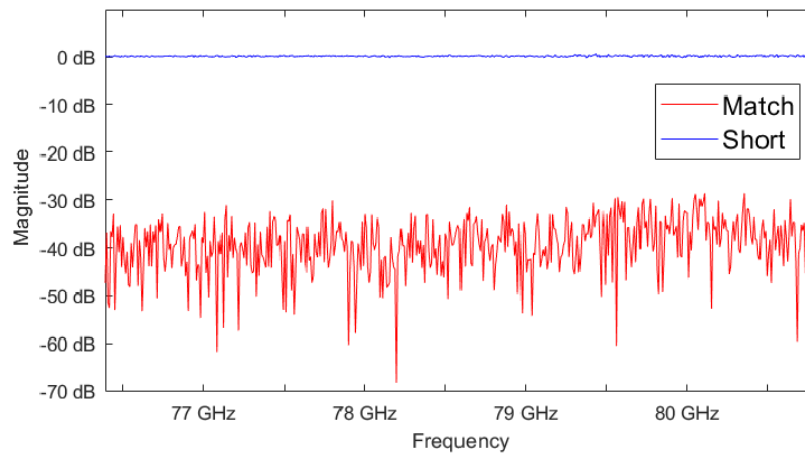


**Figure 16.** Magnitude of  $\Gamma_{in}$  for match and short measurements.

## 5.2. Measurement Results

In order to validate our theory, two different dielectric materials with different dielectric properties and thicknesses are tested. The first material tested is high-density polyethylene (HDPE) which is a common plastic material used for manufacturing pipes and bottles. This material has a dielectric constant  $\epsilon_r$  of 2.3 and a loss tangent  $\tan \delta$  of 0.0003 [2]. The sample used for testing is a  $12'' \times 12''$  plate with  $1''$  thickness. The sample is fixed on the wooden holder as seen in Figure 17(a).

The extracted magnitude and phase of the input reflection coefficient  $\Gamma_{in}$  of the HDPE material over the frequency band from 76.38 GHz to 80.8 GHz are shown in Figure 18. This bandwidth represents the maximum effective sweeping bandwidth of the used radar board.

The above results prove the effectiveness of the calibration process with minimal magnitude distortion and a clean linear phase.

Using the maxima and minima method, the extracted dielectric constant is calculated to be 2.44. By using the frequency difference between the maxima and minima of  $\Gamma_{in}$ , the order of the maximum is found to be equal to 21. Moreover, the thickness is calculated to be 2.63 cm using Equation (47) and the extracted dielectric constant and the order of the maximum. Finally, these extracted parameters are used as initial values for the nonlinear least square curve fitting method for the magnitude and phase of  $\Gamma_{in}$  using Equations (50) and (51). The dielectric parameters and thickness extraction results for the HDPE sample are shown in Table 1 using the 3 different extraction methods compared against actual



**Figure 17.** Material sample used for the test (a) HDPE, (b) PMMA.

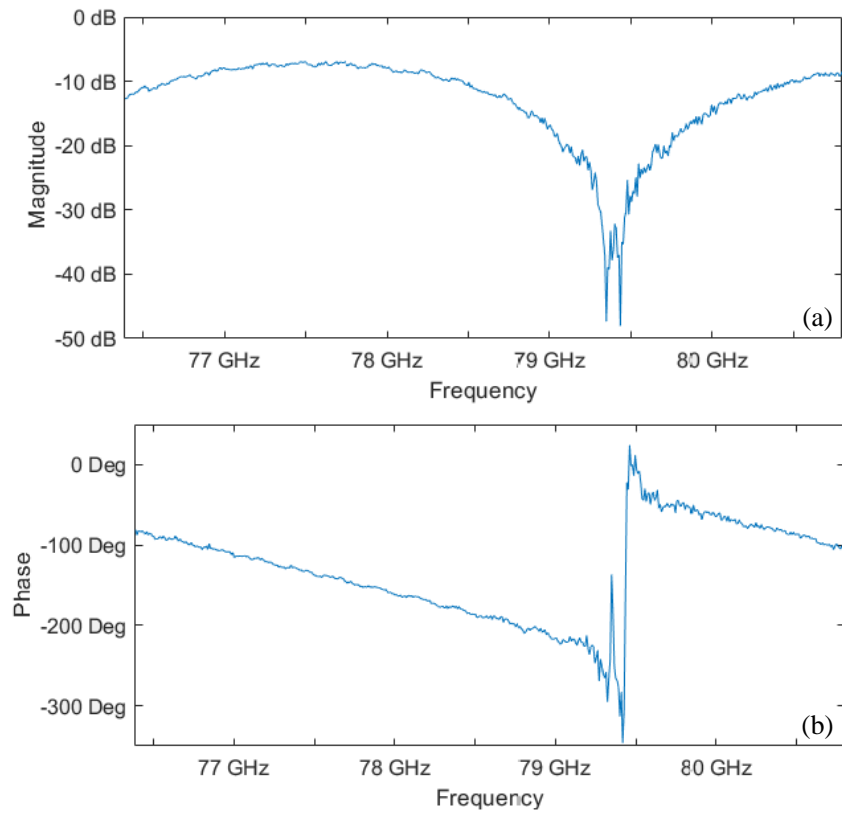


**Figure 18.** Measured (a) magnitude and (b) unwrapped phase of  $\Gamma_{in}$  for a 12'' × 12'' × 1'' HDPE sample.

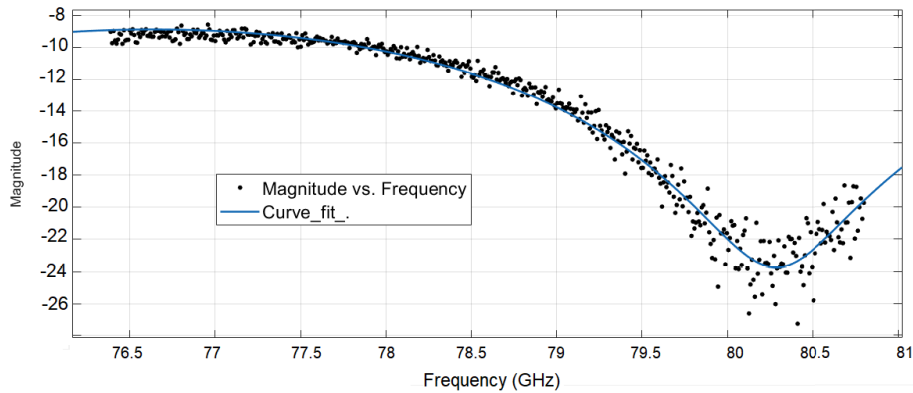
thickness and dielectric parameters from literature.

While the maxima and minima method is simple and fast to compute, it can be noted from the results that the curve fitting method using the magnitude or phase provides more accuracy. Additionally, while the maxima and minima method only works for lossless dielectric materials, the curve fitting method can be applied to both lossy and lossless materials.

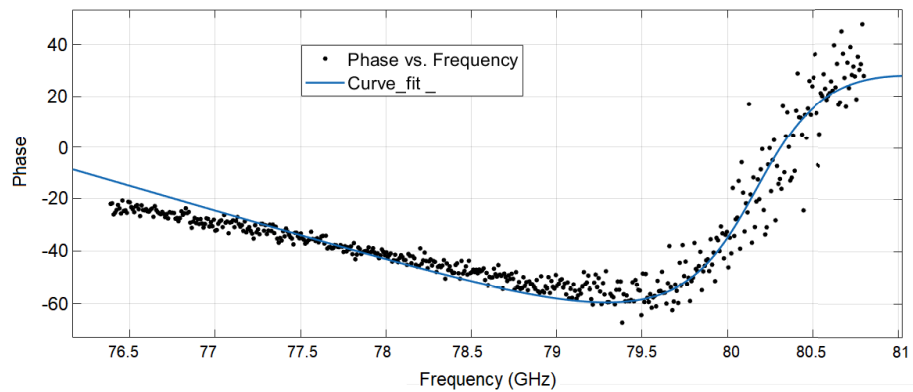
The second sample measured is a 12'' × 12'' polymethyl methacrylate (PMMA) slab with 0.5'' thickness. This dielectric material has a dielectric constant  $\epsilon_r$  of 2.6 and a loss tangent  $\tan \delta$  of 0.012 [2]. Similar to HDPE sample testing, the PMMA slab is placed on the holder as seen in Figure 17(b), and the input reflection coefficient  $\Gamma_{in}$  is measured after calibrating the measurement setup. The extracted

**Table 1.** Measurement results for HDPE sample.

	$\epsilon_r$	$\tan\delta$	$d$ (cm)
<b>Maxima and Minima</b>	2.44	N/A	2.63
<b>Curve Fit (Magnitude)</b>	2.378	0.0008	2.57
<b>Curve Fit (Phase)</b>	2.27	0.0004	2.5
<b>Actual</b>	2.3	0.0003	2.54 (1")



(a)



(b)

**Figure 19.** Curve fitting on the magnitude and phase of  $\Gamma_{in}$  for the PMMA sample.

magnitude and phase of  $\Gamma_{in}$  of the slab along with the curve fit are presented in Figure 19.

Using the maxima and minima method, the dielectric constant  $\epsilon_r$  and the thickness of the slab are found to be 2.08 and 1.49 cm, respectively. These values are then used as initial values for the curve fitting method. The extracted parameters using the two methods are compared in Table 2.

It can be noted that the accuracy of the maxima and minima method is lower for PMMA due to the relatively higher losses in the material and the assumption of a lossless dielectric for that extraction method. Furthermore, the slight deviation between the phase of  $\Gamma_{in}$  and the phase curve fit in Figure 19 is due to the sensitivity of the linear phase distortion term in Equation (36) to calibration errors.

Table 3 summarizes a comparison between our work and other recent free-space material characterization methods.

Future work includes implementing a machine learning based material classification model to quickly identify the type of the material based on the extracted dielectric parameters.

**Table 2.** Measurement results for PMMA sample.

	$\epsilon_r$	$\tan\delta$	$d$ (cm)
<b>Maxima and Minima</b>	2.08	N/A	1.49
<b>Curve Fit (Magnitude)</b>	2.4	0.0099	1.32
<b>Curve Fit (Phase)</b>	2.5	0.0099	1.3
<b>Actual</b>	2.6	0.012	1.3 (0.5")

**Table 3.** Comparison between this work and other free-space characterization techniques.

Ref.	Meas. distance	Cost	Environment	Meas. device	Mobility
[16]	15 cm	Very high	Laboratory	Oscilloscope	Low
[17]	1.25 m	Very high	Multipath	VNA	Low
[18]	1 m	High (Custom)	Laboratory	Custom FMCW	Low (Fixed)
[26]	61 cm	Very high	Laboratory	VNA	Low
[27]	3 mm	Very high	Anechoic	VNA	Low
This work	2 m	Low	Multipath	Commercial FMCW	High

## 6. CONCLUSION

A remote material characterization technique using a complex-baseband FMCW radar is presented. Two equivalent models for a flat dielectric slab with finite thickness are introduced with the formulas for the input reflection coefficients  $\Gamma_{in}$  at the surface of the slab. A further theoretical analysis proves the existence of the complex input reflection coefficient of the material in the complex baseband FMCW signal of the radar. Two different dielectric parameters extraction methods are presented, the maxima and minima method and the curve fitting method. The utilization of both the magnitude and phase of the input reflection coefficient improves the accuracy of the measurement and provides additional information regarding the layer configuration. The commercial off-the-shelf TI AWR2243 radar board with a custom designed dielectric lens is used for the experimental measurement setup for validating the material characterization technique. Finally, two different material samples are tested, HDPE and PMMA. The dielectric parameters extracted using the maxima and minima method are used as initial fitting values for the curve fitting method on the magnitude and phase for enhancing the accuracy. While the maxima and minima method is only effective for lossless dielectric samples, the curve fitting method can be used for both lossy and lossless materials. The measurement results confirm the effectiveness and accuracy of the proposed remote material characterization technique and the dielectric parameter extraction methods.

## REFERENCES

1. Wagner, J., J. C. Barowski, and I. Rolfes, "A 3D printed elliptical mirror for material characterization using FMCW transceivers," *Asia-Pacific Microwave Conference (APMC)*, 1–3, 2018, doi: 10.23919/APMC.2018.8617212.
2. Yaw, J. C., "Measurement of dielectric material properties, application note," *Rohde & Schwarz*, 2012.
3. Junqueira, C., M. Perotoni, and D. R. Lima, "Microwave absorber materials characterization: Bulk absorbing and electrical/magnetic parameters," *2014 Inter. Telecom. Symposium (ITS)*, 1–5, 2014, doi: 10.1109/ITS.2014.6948015.

4. Zahid, A., H. T. Abbas, F. Sheikh, T. Kaiser, A. Zoha, M. Imran, and Q. H. Abbasi, "Monitoring health status and quality assessment of leaves using terahertz frequency," *IEEE International Symposium on Antennas and Propagation and USNC-URSI Radio Science Meeting*, 1–2, 2019, doi: 10.1109/APUSNCURSINRSM.2019.8889356.
5. Aouabdia, N., B. Tahar, N. Eddine, and G. Alquié, "Rectangular patch resonator sensors for characterization of biological materials," *IEEE 11th International Multi-Conference on Systems, Signals & Devices (SSD14)*, 1–2, 2014, doi: 10.1109/SSD.2014.6808748.
6. Obol, M., N. Al-Moayed, S. Naber, and M. Afsar, "Using coaxial probe for broadband microwave characterization of biological tissues," *38th European Microwave Conference*, 1–4, 2008, doi: 10.1109/EUMC.2008.4751477.
7. Samir, A., H. El-Sherif, S. Kishk, M. M. Abdel-Razzak, and M. Basha, "Linear and nonlinear properties of graphene at millimeter-wave for multiplier and mixer applications," *Progress In Electromagnetics Research C*, Vol. 81, 141–149, 2018.
8. Bronckers, L. A. and A. B. Smolders, "Broadband material characterization method using a CPW with a novel calibration technique," *IEEE Antennas and Wireless Propagation Letters*, Vol. 15, 1763–1766, 2016, doi: 10.1109/LAWP.2016.2535115.
9. Kazempour, A., S. K. Yee, M. Hudlička, M. Salhi, T. Kleine-Ostmann, and T. Schrader, "Design and calibration of a compact quasi-optical system for material characterization in millimeter/sub-millimeter wave domain," *IEEE Transactions on Instrumentation and Measurement*, Vol. 64, No. 6, 1438–1445, 2014, doi: 10.1109/TIM.2014.2376115.
10. Havrilla, M. and D. Nyquist, "Electromagnetic characterization of layered materials via direct and de-embed methods," *IEEE Transactions on Instrumentation and Measurement*, Vol. 55, No. 1, 158–163, 2006, doi: 10.1109/TIM.2005.861249.
11. You, K. Y., *Microwave Systems and Applications*, 1–434, IntechOpen, 2016.
12. Boybay, M. S. and O. M. Ramahi, "Material characterization using complementary split-ring resonators," *IEEE Transactions on Instrumentation and Measurement*, Vol. 61, No. 11, 3039–3046, 2012, doi: 10.1109/TIM.2012.2203450.
13. Jha, A. K. and M. J. Akhtar, "Cavity based RF sensor for dielectric characterization of liquids," *2014 IEEE Conference on Antenna Measurements & Applications (CAMA)*, 1–4, 2014, doi: 10.1109/CAMA.2014.7003427.
14. Obrzut, J., A. Hassan, and E. Garboczi, "Free space microwave non destructive characterization of composite materials," *Proceedings of the ASNT, NDT of Composites*, 1–4, 2015.
15. Will, B. and I. Rolfes, "Application of the thru-network-line self-calibration method for free space material characterizations," *2012 International Conference on Electromagnetics in Advanced Applications*, 1–4, 2012, doi: 10.1109/ICEAA.2012.6328749.
16. Chan, K. K., A. E. Tan, L. Li, and K. Rambabu, "Material characterization of arbitrarily shaped dielectrics based on reflected pulse characteristics," *IEEE Transactions on Microwave Theory and Techniques*, Vol. 63, No. 5, 1700–1709, 2015, doi: 10.1109/TMTT.2015.2418199.
17. Pometcu, L., A. Sharaiha, R. Benzerga, R. D. Tamas, and P. Pouliguen, "Method for material characterization in a non-anechoic environment," *Applied Physics Letters*, Vol. 108, No. 16, 2016, doi: <https://doi.org/10.1063/1.4947100>.
18. Barowski, J., M. Zimmermanns, and I. Rolfes, "Millimeter-wave characterization of dielectric materials using calibrated FMCW transceivers," *IEEE Transactions on Microwave Theory and Techniques*, Vol. 66, No. 8, 3683–3689, 2018, doi: 10.1109/TMTT.2018.2854180.
19. Hegazy, A. M., "Remote material characterization using mmWave FMCW radar with complex baseband," MASC Thesis, UWSpace, 2021, uri: <http://hdl.handle.net/10012/16652>.
20. Balanis, C. A., *Advanced Engineering Electromagnetics*, 2nd Edition, Wiley, 2012.
21. Ramasubramanian, K. and B. Ginsburg, "AWR1243 sensor: Highly integrated 76–81-GHz radar front-end for emerging ADAS applications," *Texas Instruments, White Paper*, 2017.
22. Stove, A., "Linear FMCW radar techniques," *Proceedings of the IEEE*, Vol. 139, No. 5, 1992, doi: 10.1049/ip-f-2.1992.0048.

23. "AWR2243 single-chip 76- to 81-GHz FMCW transceiver," *Texas Instruments, Datasheet*, 2020.
24. Ramasubramanian, "Using a complex-baseband architecture in FMCW radar systems," *Texas Instruments, White Paper*, 2017.
25. Hegazy, A. M., M. Alizadeh, A. Samir, M. Chavoshi, M. A. Basha, and S. Safavi-Naeini, "3D-printed mmWave dual dielectric lens antenna for series-fed arrays," *2022 IEEE International Symposium on Antennas and Propagation and USNC-URSI Radio Science Meeting*, 1–2, 2022, doi: 10.1109/AP-S/USNC-URSI47032.2022.9887287.
26. Vohra, N., J. S. Batista, and M. El-Shenawee, "Characterization of radar absorbing materials at 75 GHz–90 GHz using free-space system," *IEEE International Symposium on Antennas and Propagation and North American Radio Science Meeting*, 1–2, 2020, doi: 10.1109/IEEECONF35879.2020.9330271.
27. Martinez, D. P., D. R. Somolinos, and B. P. Gallardo, "Electromagnetic characterization of materials through high accuracy free space measurements," *15th European Conference on Antennas and Propagation (EuCAP)*, 1–2, 2021, doi: 10.23919/EuCAP51087.2021.9411297.